Solidification of kaolinitic clay via the adoption of reactive magnesia, quicklime, sodium carbonate and early-age oven curing

Shaoqin Ruan[a,b], Shuang Liang[b], Gediminas Kastiukas[b,c]*, Weiping Zhu[d], Xiangming Zhou[b,]*

[a]College of Civil Engineering and Architecture, Zhejiang University, Hangzhou, 310058, PR China

[b]Department of Civil and Environmental Engineering, Brunel University London, Uxbridge, Middlesex UB8 3PH, United Kingdom

[c]Guangdong Provincial Key Laboratory of Durability for Marine Civil Engineering, Shenzhen University, Shenzhen, 518060, PR China

[d]Whitireia New Zealand 450 Queen St, Auckland CBD, Auckland 1010

*Corresponding author. E-mail: Gediminas.Kastiukas@brunel.ac.uk (G. Kastiukas); Xiangming.Zhou@brunel.ac.uk (X. Zhou);

Abstract: This study introduced quicklime (i.e., CaO), reactive magnesia (i.e., MgO) and sodium carbonate, together with an early-age oven curing regime as an approach of kaolinitic clay solidification, and their strength development was measured and later interpreted by the subsequent tests including pH test, porosity measurement, Fourier-Transform Infrared Spectroscopy (FTIR), X-ray diffraction (XRD) and scanning electron microscopy-Energy-dispersive X-ray spectroscopy (SEM-EDX). Besides, the environmental impacts with respect to the production of additives for clay solidification were also calculated. The results indicated that the incorporation of CaO and MgO effectively solidified the clay with acceptable compressive strength (CaO group: 12.2 MPa; MgO group: 20.3 MPa after 28 days). Meanwhile, given the strength development of samples investigated in this study, the morphology of hydration phases could be possibly more important than their contents and sample porosity. Further, with the 3 days of oven curing introduced, MgO took advantage over CaO in clay solidification, which can be attributed to the

formation of fibrous crystals (i.e., nesquehonite) and fewer micro-cracks presented within the samples. Finally, from a perspective of 'greenness' and sustainability, MgO is a more favorable additive than CaO and PC in soil solidification.

Keywords: Clay solidification; Quicklime; Reactive Magnesia; Microstructure; Environmental impacts

1. Introduction

To reduce the Portland cement usage, which is one of the major contributors to the climate change, supplementary cementitious materials (SCMs) including blast-furnace slag, fly ash, silica fume, calcined clays and natural pozzolans, have been widely adopted in concrete formulations, either in blended cements or incorporated separately in the concrete mixer [1]. These materials, when used as mineral admixtures in concrete, can improve either or both the strength and durability properties of concrete due to the formation of C-S-H or C-A-S-H [2]. Meanwhile, some natural pozzolans such as kaolinite has also been solidified via the use of PC, which is employed in the construction of road pavements due to the considerable environmental and economic benefits [3]. As a result, the strength of clay is greatly improved through some hydration phases (e.g., C-S-H) produced within samples [4, 5]. However, the introduction of PC in the clay solidification raises an environmental concern as PC is produced at a very high temperature (i.e., 1450 ºC) and emits a large amount of CO_2 during this calcination [6-8]. At the same time, some other strong alkali were also been chosen in clay solidification such as NaOH at a Na/Si ratio of 0.8-1, and this technique has been widely investigated and applied into the road in some developing countries [9, 10], and the highest strength (i.e., 32 MPa) revealed in samples with 16% of NaOH mixed, which was cured at 80 °C for 24 hours [9]. Meanwhile, steam curing may also facilitate the strength development of alkali-activated calcined clay samples. For instance, the compressive strength of 6M NaOH-activated samples reached 12.4

MPa and 20 MPa after 2 days and 28 days respectively with the introduction of steam curing [11]. Nevertheless, production of strong alkali as well accounts for heavy environmental burdens owing to its high energy consumption, albeit it is introduced in clay solidification at a low dosage [12]. Moreover, lime has been widely adopted as well in the area of soil solidification [13-15], and the process of clay solidification may sometimes be coupled with the incorporation of ground granulated blast-furnace slag (GGBS) into clay. For instance, Consoli et al. [16] indicated that in an ambient temperature, the lowest level of lime with regard to the clay solidification was 3 wt. %, which led to a great improvement of strength (i.e., > 2 MPa).

Recently, another promising mineral additive, reactive magnesia has also been proposed in soil solidification [17-23], which is normally derived from the calcination of magnesite (i.e., $MgCO_3$) at a lower calcination temperature ranging from 700–1000 °C, thus its production process is more sustainable than PC production (i.e., 1450 °C) [6, 24]. In addition, involvement of magnesia for soil solidification is proved to effective. For instance, Yi et al. [18] investigated the influence of magnesia with different reactivity on GGBS-clay samples and they reported that the efficiency of clay solidification was greatly enhanced in the samples containing more reactive MgO, and their strength was greatly enhanced after 28 days of normal curing (from 0.2 MPa to 1.4 MPa). Meanwhile, several studies also used CaO and MgO in soil solidification simultaneously, and Gu et al. [17] demonstrated that with the growth of MgO/CaO ratios, there was also an increment on the residual strength of clay samples subjected to various soaking regimes, that is, from < 1 MPa to around 1 MPa.

Instead of the usage of additives, some curing regimes such as a high-temperature curing have also been widely accepted in soil solidification, which is proved to be effective [9, 25]. At the meantime, accelerated CO_2 curing was also adopted to solidify the contaminated soil facilitated by the use of magnesia, and the strength of contaminated soil were greatly improved with an effective stabilization of heavy

metals consequently [26, 27]. The steady strength development of samples through accelerated carbonation can be assigned to the formation of hydrated magnesium carbonates (HMCs) [28-31]. However, carbonation process only occurs on the surface of samples, and the dense layer formed on the surface then inhibits the further procession of carbonation and the corresponding strength development of samples [32-35].

Given the foregoing, instead of using a large quantity of strong alkali such as NaOH in clay solidification, this study adopted some mineral additives including quicklime (i.e., CaO) and reactive magnesia (i.e., MgO), which are also capable of providing an alkaline environment in clay solidification. Moreover, different from the previous studies, which introduced an accelerated carbonation curing to promote the strength development of soil, this study took advantage of the formation of carbonates via the reactions between CO_3^{2-} ions and Ca^{2+}/Mg^{2+} ions within the clay samples. The CO_3^{2-} ions were derived from the dissolution of Na_2CO_3, which is externally included in clay at a very low dosage. In addition, the Na_2CO_3 in this study is also capable of providing some OH^- ions to promote the dissolution of clay particles, although its content in clay was quite low. The Ca^{2+}/Mg^{2+} ions in this study were sourced from the hydration of additives included in clay. Besides, to fasten the hydration process and strength development within the laboratory, some MgO- or CaO-based clay samples were then subjected to an oven curing for up to 3 days. The compressive strength of samples up to 28 days was measured, and the strength results were later interpreted by pH measurement, porosity, x-ray Diffraction (XRD), Fourier-transform infrared (FTIR) and scanning electron microscopy (SEM)-Energy-dispersive x-ray spectroscopy (EDX). Finally, a comprehensive environmental assessment regarding the production of additives, which are used in soil solidification, is scarce according to the previous literature, and the detailed assessment was performed in this study.

2. Materials, sample preparation and methods

2.1. Materials

The kaolinitic clay used in this study was obtained from Poland, and its chemical formulation obtained from X-ray fluorescence (XRF) spectrometry is shown in Table 1. Sodium carbonate (Na_2CO_3) with a purity of > 99% was used, provided by Sigma-Aldrich, United Kingdom. Two mineral additives, quicklime and reactive magnesia were used to replace 20 wt. % of clay during sample preparation. The primary consideration with regard to the selection of this replacement level (i.e., 20%) is to reduce the usage of magnesia and quicklime, while providing a high alkaline environment at the same time within the samples. The type and brand of quicklime (SSA: 0.9 cm^2/gram) were Limelite NHL 3.5 acquired from Tarmac, United Kingdom, and the reactive magnesia (SSA: 0.3 m^2/gram) was sourced from Magnesia GmBH, Germany, with a purity of > 95%.

2.2. Sample preparation

To reduce the content of strong alkali used clay solidification, only 10 wt. % of Na_2CO_3 compared with total solids was mixed with water, which provides some CO_3^{2-} ions and an alkaline environment at the same time. A control group was selected which contained 100 wt. % of clay, whereas for the other two groups, 20 wt. % of clay was replaced by the use of quicklime or magnesia, respectively. The w/b ratios of all three groups were chosen accordingly to ensure the same workability of fresh paste. After mixing, the pastes were cast into 50 × 50 × 50 mm^3 cubic molds, compacted via a vibrating table and trowel finished. All samples were demolded after 24 hours, and two curing regimes were adopted: (1) The samples were cured in a natural environment (i.e., temperature: 25 °C ± 1 °C; Relative humidity: 60 % ± 5 %) up to 28 days; (2) The samples were cured in an oven (i.e., 80 ºC) first for 3 days and then in a natural environment (i.e., temperature: 25 °C ± 1 °C; Relative humidity: 60 % ± 5 %) up to 28 days (i.e., 25 days of natural curing).

The mix formulations of all groups studied and their curing regimes are shown in Table 2.

2.3. Methods

2.3.1. pH values

After compression test, the crushed samples were ground to fine powders for measurement with a calibrated Mettler Toledo pH meter according to ASTM C25 [36]. A solution of 5 grams of sample powders mixed with 100 grams of distilled water was prepared and mixed for 30 minutes prior to each measurement of pH.

2.3.2. Compressive strength

For each group, three samples were tested and subjected to compression testing at 7, 14 and 28 days in line with ASTM C109/C109M-13 [37]. A 50-kN Instron 5960 universal testing machine was used at a loading rate of 12.7 mm/min.

2.3.3. Porosity

The porosity of selected clay samples was obtained via the calculation of Equation 1, which is derived from ASTM C642 [38], in which the void volume is difference between M_{sat} and M_{dry}. M_{sat} is the mass of sample saturated in water; M_{dry} is the sample mass dried at a temperature of 70 °C to constant mass; V is the volume of the sample measured by a Vernier scale.

$$P=\text{Void volume/Total volume}=(M_{sat}-M_{dry})/V*100\% \quad \text{(Eq. 1)}$$

2.3.4. XRD, FTIR and SEM-EDX

The in-situ microstructural analysis was performed, and samples extracted from the cubes crushed during the compression test were immediately investigated via XRD, FTIR and SEM/EDX. The XRD patterns of all samples were obtained using a Bruker D8-Advance X-ray diffractometer with Cu Kα radiation (λ=1.5418 Å), an operational voltage of 40 kV, a current of 40 mA and a scanning rate of 2° 2θ /step from 5 to 80° 2θ. The Fourier transform infrared (FTIR) curves with spectral subtraction were obtained in a Shimadzu IRAffinity-1 fitted with a Specac Quest attenuated total reflectance (ATR) accessory. The curves were recorded from 650 to 1650 cm^{-1} with a 2 cm^{-1} resolution, and a scan count of 25 at a scanning rate of 5-kHz was used. During the SEM analysis, the chunk samples around 5 mm*5 mm*5mm after compression test were chosen and impregnated with ultralow-viscosity resin and polished by a series of graded polishing papers and diamond paste, and the grinder used in this study is PlanarMet 300 from Buehler Esslingen, Germany. The samples were coated with gold and a high vacuum mode was used during SEM analysis. The backscattered secondary electron (BSE) images were acquired using a Zeiss Supra 35VP SEM, facilitated by the use of an energy-dispersive X-ray (EDX) analyzer.

2.3.5. Environmental impacts

The goal of this section was to obtain the environmental impacts associated with 1 kg of quicklime and magnesia production based on a European case study, and the outcomes were compared with those of PC production, which is a commonly used additive in clay solidification. Since there are no inventories of reactive magnesia in the database, the inputs and outputs owing to the production of reactive magnesia were obtained from the references [6, 39], as shown in Table 3, while the inventories of quicklime production were acquired from the Ecoinvent database. The inventories resulting from PC production were sourced from several European literature [40-44], as indicated in Table 4. A commonly used assessment approach, Eco-indicator 99, was applied in the evaluation of environmental

impacts for the additives used in soil solidification, which is capable of gaining a series of indicators such as climate change.

3. Results

3.1 pH values

The 7-day, 14-day and 28-day pH values of all samples subjected to the natural and mixed curing regimes are presented in Fig. 1. Irrespective of curing ages, compared with the pH values shown in the control group (i.e., 12.3~13.0), there is a distinct increase in the values shown in the CaO- and MgO-based clay samples, ranging from 13.3 to 14.9. In the meantime, it is clear that the CaO-based samples produced a more alkaline environment than the MgO-based counterparts, which could be explained by the following mechanisms: (1) The $Ca(OH)_2$ formed due to the hydration of quicklime reveals a greater solubility (i.e., $K_{sp}=5.5\times10^{-6}$) than $Mg(OH)_2$ (i.e., $K_{sp}=1.5\times10^{-11}$) in room temperature, and the corresponding reactions are shown in Equation 2-3. Therefore, compared with $Ca(OH)_2$ in the L20-OC and L20-NC groups, the smaller quantity of OH^- ions released by $Mg(OH)_2$ brought about the lower pH values within the clay samples; (2) Another possible explanation could be related with a higher content of hydration phases formed in the MgO-based samples (i.e., M20-OC and M20-NC), and these hydration phases could then consume or absorb more alkali within the clay samples, which led to the smaller pH values presented in these groups than the CaO-based counterparts (Fig. 1), and the above findings were also supported in the previous studies [45, 46]. However, the first explanation seems to be a more reasonable interpretation considering the later results. From the figure, it is also interesting to be noted that, except for the control group, the mixed curing regime, which introduced an oven curing at the beginning, also led to the lower pH values shown in these samples than the natural curing groups, which could be ascribed to the higher content of hydration phases formed (i.e., more alkali consumed or absorbed) under this

regime within the samples, facilitated by the faster hydration kinetics resulting from the elevated temperature, and the outcomes were also well explained by the subsequent experiments in this study. Besides, from Fig. 1, it is also obvious that the pH values of all samples fluctuated over time, and a possible interpretation could be related to the carbonation of samples, which resulted from the reaction between the hydration phases and atmospheric CO_2 in the clay samples, thus their pH equilibrium were influenced correspondingly.

$$CaO+H_2O \rightarrow Ca(OH)_2 \rightarrow Ca^{2+}+2OH^- \quad \text{(Eq. 2)}$$

$$MgO+H_2O \rightarrow Mg(OH)_2 \leftrightarrow Mg^{2+}+2OH^- \quad \text{(Eq. 3)}$$

In practice, the high pH of the soil may have an adverse effect on the plant growing and the activity of the micro-organisms within the soil. However, the main purpose of using these additives including magnesia and quicklime into clay is to solidify the clay in the construction of road pavement, where the plant growing or the activity of the micro-organisms were not considered as important indicators, and PC and CaO were the most widely used stabilizing agents in the construction of road pavements[3].

3.2. Compressive strength and porosity

Up to 28 days, the compressive strength of CaO- and MgO-based clay samples is shown in Fig. 2, where the natural and mixed curing regimes were adopted. The figure clearly indicated that regardless of the curing regimes adopted, the strength of control groups without any mineral additives (i.e., the C-NC and C-OC group) is relatively weak (i.e., close to 0 MPa) even after 28 days of curing, and the C-OC group performed only slightly better than the C-NC group concerning the strength development, which is related to their relatively porous structures, as shown in Fig. 3(a). As indicated by a previous study [9], coupled with an elevated temperature curing, a strongly alkaline environment is required to dissolve the alumino-silicate

in clay, and a Na/Si ratio of 0.8-1 is a necessity in clay solidification, whereas the Na/Si ratio in this study was only about 0.2, which resulted in a low efficiency of clay solidification due to the insufficient pH provided by the sole usage of 10 wt. % Na_2CO_3 in clay, as discussed in Section 3.1. When it comes to the strength results of samples subjected to the natural curing regime (i.e., L20-NC and M20-NC group), given the 7-day and 14-day compressive strength, the CaO-based clay samples outperformed the MgO-based counterparts, and the higher pH values revealed in L20-NC (Fig. 1) may explain the variations, which resulted in a better hydration behavior of clay particles and greater strength achieved in the L20-NC group, however, after 28 days of natural curing, both the CaO- and MgO-based samples demonstrated similar compressive strength (i.e., 10 MPa), which could be interpreted by the improvement in the homogeneity of hydration phase distribution, when a higher content of magnesia replacement was introduced in clay samples [17].

For the mixed curing regime, Fig. 2 also clearly reveals that the M20-OC group presents superior compressive strength than that of the L20-OC group. For instance, after 28 days of mixed curing, the average compressive strength revealed by the M20-OC group is 20.4 MPa, which is 110% greater than that of the L20-OC group. It is widely accepted that strength among samples is highly related to porosity, and the formed hydration phases would fill in the pores within the mixture, which led to a more compacted structure and better strength of samples [47]. However, this theory may not be applied in this study, as a quite similar sample porosity (i.e., around 27 %) was both observed in the CaO- and MgO-based clay samples, as shown in Table 5. Considering this, a possible interpretation of strength difference between the M20-OC and the L20-OC groups could be resulting from the varying morphology of hydration phases, which will be explained in the later sections. Besides, another cause of inferior compressive strength observed in the L20-OC group can be assigned to the occurrence of micro-cracks in samples (Fig. 3(b)) due to the oven curing (or drying), although this curing regime may also promote the hydration of precursors [48], whereas a

different surface image was observed in the M20-OC group (Fig. 3(b)), which could be associated with the volume expansion of samples owing to the magnesia hydration [49], and its delayed hydration, which was resulted from its low solubility, reduced the probability of micro-cracks formation as a consequence of thermal shrinkage at a later curing age [50-52]. For the quicklime, although it was also used as a type of expansive additive, however, the rapid reaction of CaO with water, as well as its potential hydration during storage even in a natural environment, reduced its expansion efficiency in concrete [53].

In view of the strength results presented in Fig. 2, some of the mixtures meet the 7-day strength requirement (i.e., 3~5 MPa) stipulated by the Chinese standard [54] in terms of the construction of roadbases in highway.

3.3 XRD

The XRD patterns of the C-OC, L20-OC, M20-OC and M20-NC groups under the mixed curing regime were shown in Fig. 4(a) and (b). Within all the groups investigated, the presence of quartz and kaolinite can be found even after 28 days of mixed curing, and these phases are derived from the clay, as seen from Table 1. The table also shows that the C-S-H together with the calcite ($CaCO_3$) is detected (28-29° 2θ) in the patterns of the L20-OC group, and this finding is also in line with a previous reference [18]. For the M20-OC group, the peak of 28-29° 2θ can be ascribed to the presence of nesquehonite ($MgCO_3 \cdot 3H_2O$), yet the presence of M-S-H in this mixture is still uncertain, which is due to its amorphous nature and broad hump shown in the XRD patterns [45, 55]. Meanwhile, the clay used in this study is also almost free of CaO content (Table 1), thus the possibility of calcium-bearing phases in the M20-OC group could be eliminated, which is also confirmed by the XRD pattern of the C-OC group in Fig. 4(a) since the peaks of C-S-H or calcite were both absent. Further, Fig. 4(a) also indicated the absence of portlandite ($CaOH)_2$) or brucite ($Mg(OH)_2$) from the patterns, revealing that after 28

days of curing, the Ca^{2+} and Mg^{2+} ions may be completely involved in the formation of Ca- and Mg-containing phases within the clay samples under an alkaline environment, and the outcomes were also in accordance with several previous investigations [56-58]. In addition, the corresponding peaks of Na_2CO_3 cannot be identified from all the XRD patterns, showing its complete dissolution within the samples after 28 days of curing, and the resultant CO_3^{2-} ions in the pore solution were then involved in the formation of calcite or nesquehonite at a later stage.

The XRD patterns of the M20-OC and M20-NC groups is presented in Fig. 4(b). The patterns obviously indicate that the oven curing at an early stage facilitated the formation of nesquehonite ($MgCO_3 \cdot 3H_2O$), which could also be assigned to the better dissolution of magnesia facilitated by elevated-temperature, whose solubility is quite low in room temperature. Therefore, in comparison with the L20-OC group, the introduction of oven curing at an early age promoted the formation of more Mg^{2+} ions, which would readily react with CO_3^{2-} in the pore solution and a larger quantity of nesquehonite was produced as a result in the M20-OC group, which enhanced the strength of samples subjected to the mixed curing, and the details of nesquehonite formation can be found in the section of Discussion.

3.4. FTIR

The FTIR spectra of clay, quicklime, magnesia and selected clay samples subjected to the mixed curing regime are presented in Fig. 5(a). The spectra of the L20-OC and M20-OC groups indicate a peak at 800-1200 cm^{-1}, though they present different shapes and locations (i.e., peak center) when compared with the C-OC group and precursor, which is mainly attributed to the Si-O bond [59]. In addition to the stretching vibrations of Si-O, the 870 cm^{-1} bands in the L20-OC and M20-OC groups can be ascribed to the bending band of CO_3^{2-} ions, which was usually reported at around 875 cm^{-1} [60]. In view that the Na_2CO_3 was totally dissolved in these clay samples after 28 days of curing, the bending band of CO_3^{2-}

ions also confirms the presence of calcite ($CaCO_3$) or nesquehonite ($MgCO_3 \cdot 3H_2O$), as shown in Fig. 4. In the C-OC, M20-OC and L20-OC groups, the circled portions between 1070 cm^{-1} and 1210 cm^{-1} are related to the presence of clay, but the remainders ranging from 800 cm^{-1} to 1070 cm^{-1} display the presence of some hydration phases produced within the C-OC, L2O-OC and M20-OC groups, which are different from the precursor. Therefore, for a more clear comparison, the produced phases was conservatively estimated by a spectral subtraction (with linear baseline correction applied), as indicated in Fig. 5(b). The figure shows that the produced phases reveal their main peaks between 960 cm^{-1} and 980 cm^{-1}, which can be assigned to the presence of some hydration products (i.e., C-S-H or M-S-H possibly), and the findings were also in line with the previous studies [23, 61, 62], although the evidence of M-S-H within the M20-OC group is not very strong because of its amorphous nature, which will be discussed later. Further, the relatively low intensity of peaks within the range of 960 cm^{-1} and 980 cm^{-1} in the C-OC group reveals a scarce of hydration phases, explaining its porous structure and negligible compressive strength, which is also confirmed by the XRD patterns in this study. Besides, from Fig. 5(b), it can also be found that the L20-OC group may contain a greater quantity of hydration phases than the M20-OC group, reflected by its stronger peak intensity and larger peak area, yet the M20-OC group still outperformed the L20-OC group with regard to the compressive strength, showing that the quantity of produced phase (or porosity) is not the only factor that dominates the strength of clay samples in this study, which will be elaborated later in the section of Discussion. Finally, Fig. 5(b) has a clear representation that the three peak centers of the C20-OC, L20-OC and M20-OC groups differ slightly, ranging from 960 cm^{-1} and 980 cm^{-1}, and [63] suggested that this variation could probably be interpreted by the varying Ca/Si ratios, and a higher Ca/Si ratio in the samples was accompanied by a lower wavenumber in the FTIR curves.

3.5. SEM-EDX

Some BSE images of selected samples after 28 days of mixed curing were displayed in Fig. 6. For a fair comparison, the magnification of all SEM images were kept the same. As expected, in the C-OC group, there is a large content of unreacted quartz (i.e., SiO_2; spherical particles) left, and it is also reported that dark grey areas on BSE images refer to the presence of C-S-H in the samples [64], thus very little C-S-H is found from the BSE image in the C-OC group (Fig. 6(a)), which is also supported by the previous results. For the L20-OC group, the unreacted particles (i.e., kaolinite and quartz) are connected by some dark grey areas, which is C-S-H or possibly calcite in Fig. 6(b), and a more dense structure was seen in the L20-OC group than the C-OC group, accounting for its greater strength achieved. Besides, through the elemental spectra in Fig. 7(a), owing to the presence of carbon in the dark area, the presence of calcite ($CaCO_3$) can also be confirmed, which is intermixed with the C-S-H in the L20-OC group. While the C-S-H results from the reaction between the clay particles and the Ca^{2+} ions, the source of Ca^{2+} ions in the formation of calcite may vary, which will be discussed later.

Different from the L20-OC group, fibrous hydration products are prevailing in the M20-OC group (Fig. 6(c)), and these crystals resemble the morphology of nesquehonite ($MgCO_3{\cdot}3H_2O$) [65, 66] or natrite (Na_2CO_3) [67], however, from the XRD patterns, the possibility of natrite (Na_2CO_3) is eliminated in the M20-OC group. In addition, the elemental spectra in Fig. 7(b) also indicates the presence of carbon within the fibrous crystals, consequently, the dominant hydration phases in M20-OC can be attributed to the presence of nesquehonite ($MgCO_3{\cdot}3H_2O$), which is also in line with the XRD results. As expected, it is still very difficult to confirm the existence of M-S-H in the M20-OC group from BSE images, which will also be discussed later.

4. Discussion

The effects of quicklime incorporation on the clay solidification are pronounced. The continuous hydration of the L20-OC group led to the C-S-H produced that connected the clay particles, which resulted in a denser structure than the C-OC group. It was reported that amorphous C-S-H including C-S-H gel, C-S-H (I) and C-S-H (II) is a thermodynamic metastable phase, and the relatively low temperature led to the formation of amorphous C-S-H, whereas crystalline C-S-H can be formed including tobermorite and xonotlite at elevated-temperature [68]. Therefore, the 3-day oven curing at an early stage led to the formation of C-S-H with more crystallized structure in the clay samples. Meanwhile, from the previous sections, the calcite produced (Equation 4) is also intermixed with the C-S-H in the L20-OC group. There are two possible Ca^{2+} ion sources, that is, the hydration of CaO or the leaching of C-S-H in the L20-OC group. However, it is also clear that the crystalline C-S-H, which is formed in this study, shows greater stability than the amorphous C-S-H gel, indicating its relatively inferior capacity of Ca^{2+} ions release owing to its lower solubility [69]. Given this circumstance, it is believed that the Ca^{2+} ions in Equation 4 was mainly derived from the dissolution of mineral additive (i.e., CaO). Meanwhile, the dissolution of Na_2CO_3 is supposed to play a major role for the provision of CO_3^{2-} ions in Equation 4. Due to the low concentration of CO_2 in the air (~0.04%), only a small proportion of atmospheric CO_2 would be dissolved into the pore solution even after 28 days of curing, leading to a negligible CO_3^{2-} ions resulting from the carbonation in the L20-OC group. Another study [46] also reported that the solubility of crystalline silica (i.e., quartz) that is found in this study is several orders of magnitude lower than the amorphous silica (MS), which greatly inhibits the dissolution of clay particles as well as the formation of the C-S-H correspondingly, reflected by the lower compressive strength in the C-OC and C-NC groups. Consequently, the calcite may play a more important role than the C-S-H in the determination of compressive strength in the L20-OC group, which will be explored in the future.

$$Ca^{2+}+CO_3^{2-}\rightarrow CaCO_3 \quad \text{(Eq. 4)}$$

The benefits of magnesia incorporation in the clay solidification are also clear. Different from the formation of calcite, it is very difficult to produce magnesite (i.e., $MgCO_3$) within the samples [70], and inevitably, the Mg^{2+} ions would readily react with CO_3^{2-} ions as well as combine several molecules of H_2O to produce a series of hydrated magnesium carbonates (HMCs) with varying morphology within samples [32, 65, 66, 71]. In this study, the type of HMC that was found within the M20-OC group is identified as nesquehonite through the XRD patterns and the SEM images, and its reaction formula is shown in Equation 5:

$$Mg^{2+}+CO_3^{2-}+3H_2O \rightarrow MgCO_3 \cdot 3H_2O \quad \text{(Eq. 5)}$$

In Equation 5, the Mg^{2+} ions could be either obtained from the dissolution of $Mg(OH)_2$ or possibly M-S-H, albeit the presence of M-S-H in the M20-OC group is still in doubt, which will be investigated in the future. Besides, as aforementioned, considering the low solubility of quartz in clay, the amount of M-S-H should also be low as well, which is also confirmed by the low peak density and small peak area of produced phase than C-S-H through the FTIR curve in the M20-OC group, provided that the main peak of 960 cm^{-1} and 980 cm^{-1} was assigned to the presence of M-S-H. Further, [45] also demonstrated that the amorphous M-S-H presents a higher solubility compared with the crystalline M-S-H such as sepiolite ($Mg_4Si_6O_{15}(OH)_2 \cdot 6H_2O$) or chrysotile ($Mg_3(Si_2O_5)(OH)_4$). Therefore, in terms of the foregoing, even though M-S-H indeed formed at an early stage within the pore solution in the M20-OC group, after 28 days of curing, the leaching of Mg^{2+} ions from the M-S-H due to its good solubility may then absorb CO_3^{2-} ions and H_2O molecules to produce the HMCs. As a consequence, nesqhehonite was formed in this study. At the same time, compared with the L20-OC group, greater strength was observed in the M20-OC group owing to the presence of fibrous nesquehonite. The mechanical performance of brittle samples is determined by several key factors such as the quantity of hydration phases formed, which resulted in a reduction of pores and a more compacted structure within the samples. However, in view of the FTIR curves and the similar porosity results of the L20-OC and M20-

OC groups, more hydration phases were observed in the L20-OC group than the M20-OC group, whereas an opposite scenario was found concerning the compressive strength of the L20-OC and M20-OC groups, which could be interpreted by the different hydration products formed within these two groups, and the produced phases present various morphology, in other words, the morphology of hydration phases within the clay samples could possibly play a more important role than their content as well as sample porosity for the strength of samples investigated, and a similar finding was also reported in a previous study [72], where the mechanical performance of samples was also greatly influenced by the morphology of hydration phases instead of their quantity. In addition, [32, 73] proposed that the fibrous and needle-like crystal growths are more useful than the rounded or tabular crystals concerning the strength development of samples. Hence, owing to the 3D structures, the fibrous nesquehonite revealed better microstructural strength than the C-S-H/calcite mixture, and the compressive strength of the M20-OC group is much higher than that of the L20-OC group consequently. At the meantime, it is also speculated that the possible effects of interlocking resulting from the fibrous nesquehonite may further enhance the compression resistance of the MgO-based clay samples, which is also put forward in a previous reference [32]. Therefore, in consideration of the above discussion, it can be concluded that instead of the content, the morphology of hydration phases could be possibly more crucial in controlling the compressive strength of clay samples investigated in this study.

When it comes to the effects of early-age oven curing, it may present dual effects on the compressive strength of the L20-OC group. For one thing, the oven curing may facilitate the hydration behavior and the subsequent strength development of clay samples. For another, since the hydration rate of quicklime is very fast, which causes a low efficiency of expansion, the oven curing (or drying) may bring about the occurrence of micro-cracking within the samples containing quicklime at a later curing age, which would deteriorate their overall compressive strength. Nevertheless, the chances of micro-cracks formation within the M20-OC samples

were reduced by the delayed volume expansion of magnesia hydration. [51] reported that the hydration of MgO can be found on the exterior surface of their particles, inner pore surface as well as boundary, and the $Mg(OH)_2$ precipitates adjacent to the MgO particles resulting from the short diffusion distance of Mg^{2+} ions gradually, then the delayed expansion of magnesia particles can be observed consequently. Since the expansive process (i.e., hydration) of magnesia particles occurs within a confined area, which is previously dominated by the initial ones, the expansive stress is generated owing to the confined expansion, hence, the cement samples are expanded subsequently. Therefore, considering the absence of micro-cracks, when magnesia is incorporated in clay solidification, the effect of oven curing at an early stage on the strength development of clay samples could be strengthened. An illustration of chemical reactions occurred in the L20-OC and M20-OC groups is presented in Fig. 8, which also explained the strength variations between these two groups.

In terms of additives selection in soil solidification, their environmental impacts associated with the production are of great significance for the decision-makers. Therefore, an environmental assessment of quicklime, reactive magnesia and PC production was then performed in this study, which would increase the awareness of the adoption of more sustainable additives for clay solidification. It is know that there are several routes to acquire quicklime or reactive magnesia in practice. Therefore, in this study, the quicklime and reactive magnesia were both assumed to be obtained via the calcination of minerals, that is, limestone (i.e., $CaCO_3$) and magnesite (i.e., $MgCO_3$), and their calcination process are shown in Equation 6-7.

$$CaCO_3 \rightarrow CaO + CO_2 \quad \text{(Eq. 6)}$$

$$MgCO_3 \rightarrow MgO + CO_2 \quad \text{(Eq. 7)}$$

The individual environmental impact owing to 1 kg of quicklime and reactive magnesia production is presented in Fig. 9, which also consists of the outcomes resulting from 1 kg of PC production as PC is widely used in clay solidification. The

figure clearly presents that the overall environmental burdens (i.e., single score) associated with the production of reactive magnesia is 16.4% and 41.6% lower than that of quicklime and PC production, respectively, which can be ascribed to the lower score of fossil fuels resulting from its lower calcination temperature. In the meantime, a 21.3% and 77.0% increment in the scores of climate change are demonstrated in reactive magnesia production than quicklime and PC production, which could be attributed to the higher CO_2 emitted by the decomposition of magnesite. It is widely accepted that the CO_2 emissions could be divided into the direct emission (i.e., from the decomposition of raw materials) and the indirect emission (i.e., from fuel consumption) [74]. Albeit production of reactive magnesia consumes less fossil fuels that led to the lower indirect CO_2 emissions, the direct CO_2 release into air related to 1 kg of reactive magnesia manufacturing is 1.1 kg, and the value is much greater than the same quantity of quicklime (i.e., 0.78 kg) and PC production (i.e., 0.78~0.83 kg). As a consequence, compared with the production of the other two additives, a greater overall CO_2 emission (i.e., a direct plus indirect CO_2 emission) and a corresponding higher score of climate change was revealed owing to the production of reactive magnesia.

5. Conclusions and prospects

This study solidifies the clay via the incorporation of reactive magnesia, quicklime and sodium carbonate, and the efficiency of clay solidification was further enhanced by means of an oven curing at an early stage. Overall, the outcomes obtained will provide some guidance on the solidification of contaminated clay as well as the manufacturing of clay-based products such as masonry bricks. Although the mechanical performance of the samples may be the most significant property, several other properties of the clay-based samples developed such as the setting time, the durability or the geotechnical properties (e.g., Atterberg limits) are also of great importance, which will be investigated in the future. Besides, the major conclusions can be drawn as follows:

The incorporation of quicklime and magnesia into clay provided additional Ca^{2+} and Mg^{2+} ions to produce C-S-H/Calcite and nesquehonite (possibly M-S-H). In addition to its higher sustainability as an additive, introduction of magnesia led to greater compressive strength in the samples than the CaO-based counterparts, which could be possibly ascribed to (1) the interlocking effects and a 3D structure of fibrous nesquehonite produced, indicating the importance of the morphology of hydration phases; (2) the addition of magnesia reduced the chances of micro-crack occurrence in the clay samples due to its delayed hydration.

Acknowledgment

Finance support from the European Commission Horizon 2020 Research and Innovation Programme through the grant 723825 (i.e., the Green INSTRUCT project) is greatly acknowledged.

References

[1] B. Lothenbach, K. Scrivener, R. Hooton, Supplementary cementitious materials, Cement and Concrete Research 41(12) (2011) 1244-1256.

[2] A. Elahi, P. Basheer, S. Nanukuttan, Q. Khan, Mechanical and durability properties of high performance concretes containing supplementary cementitious materials, Construction and Building Materials 24(3) (2010) 292-299.

[3] P. Sherwood, Soil stabilization with cement and lime. , Her Majesty's Stationery Office (HMSO), London, UK, 1993.

[4] S.E. Schulze, J. Rickert, Suitability of natural calcined clays as supplementary cementitious material, Cement and Concrete Composites 95 (2019) 92-97.

[5] R. Gmür, K.-C. Thienel, N. Beuntner, Influence of aging conditions upon the properties of calcined clay and its performance as supplementary cementitious material, Cement and Concrete Composites 72 (2016) 114-124.

[6] S. Ruan, C. Unluer, Comparative life cycle assessment of reactive MgO and Portland cement production, Journal of Cleaner Production 137 (2016) 258-273.

[7] D. Higgins, Briefing: GGBS and sustainability, Thomas Telford Ltd, 2007.

[8] Y. Krivoborodov, S. Samchenko, Synthesis of high alumina cement based on metallurgy wastes, IOP Conference Series: Materials Science and Engineering, IOP Publishing, 2019, p. 022034.

[9] F. Slaty, H. Khoury, J. Wastiels, H. Rahier, Characterization of alkali activated kaolinitic clay, Applied Clay Science 75 (2013) 120-125.

[10] O. Cuisinier, D. Deneele, F. Masrouri, Shear strength behaviour of compacted clayey soils percolated with an alkaline solution, Engineering Geology 108(3-4) (2009) 177-188.

[11] N.R. Rakhimova, R.Z. Rakhimov, A.R. Bikmukhametov, V.P. Morozov, A.A. Eskin, T.Z. Lygina, A.M. Gubaidullina, Role of clay minerals content and calcite in alkali activation of low-grade multimineral clays, Journal of Materials in Civil Engineering 32(8) (2020) 04020198.

[12] G. Kastiukas, S. Ruan, S. Liang, X. Zhou, Development of precast geopolymer concrete via oven and microwave radiation curing with an environmental assessment, Journal of Cleaner Production (2020) 120290.
[13] A. Haque, C.K. Tang, S. Islam, P. Ranjith, H.H. Bui, Biochar sequestration in lime-slag treated synthetic soils: a green approach to ground improvement, Journal of Materials in Civil Engineering 26(12) (2014) 06014024.
[14] S. Islam, A. Haque, S. Wilson, Effects of curing environment on the strength and mineralogy of lime-GGBS–treated acid sulphate soils, Journal of Materials in Civil Engineering 26(5) (2013) 1003-1008.
[15] L. Wang, D.-W. Cho, D.C. Tsang, X. Cao, D. Hou, Z. Shen, D.S. Alessi, Y.S. Ok, C.S. Poon, Green remediation of As and Pb contaminated soil using cement-free clay-based stabilization/solidification, Environment International 126 (2019) 336-345.
[16] N.C. Consoli, R.A.Q. Samaniego, N.M.K. Villalba, Durability, strength, and stiffness of dispersive clay–lime blends, Journal of Materials in Civil Engineering 28(11) (2016) 04016124.
[17] K. Gu, F. Jin, A. Al-Tabbaa, B. Shi, C. Liu, L. Gao, Incorporation of reactive magnesia and quicklime in sustainable binders for soil stabilisation, Engineering Geology 195 (2015) 53-62.
[18] Y. Yi, L. Gu, S. Liu, F. Jin, Magnesia reactivity on activating efficacy for ground granulated blastfurnace slag for soft clay stabilisation, Applied Clay Science 126 (2016) 57-62.
[19] H.-L. Wu, F. Jin, Y.-L. Bo, Y.-J. Du, J.-X. Zheng, Leaching and microstructural properties of lead contaminated kaolin stabilized by GGBS-MgO in semi-dynamic leaching tests, Construction and Building Materials 172 (2018) 626-634.
[20] H.-L. Wu, F. Jin, J. Ni, Y.-J. Du, Engineering properties of vertical cutoff walls consisting of reactive magnesia-activated slag and bentonite: workability, strength, and hydraulic conductivity, Journal of Materials in Civil Engineering 31(11) (2019) 04019263.
[21] L. Wang, L. Chen, D.-W. Cho, D.C. Tsang, J. Yang, D. Hou, K. Baek, H.W. Kua, C.-S. Poon, Novel synergy of Si-rich minerals and reactive MgO for

stabilisation/solidification of contaminated sediment, Journal of Hazardous Materials 365 (2019) 695-706.
[22] Y. Yi, K. Lu, S. Liu, A. Al-Tabbaa, Property changes of reactive magnesia–stabilized soil subjected to forced carbonation, Canadian Geotechnical Journal 53(2) (2015) 314-325.
[23] Y. Yi, M. Liska, F. Jin, A. Al-Tabbaa, Mechanism of reactive magnesia–ground granulated blastfurnace slag (GGBS) soil stabilization, Canadian Geotechnical Journal 53(5) (2015) 773-782.
[24] S. Ruan, C. Unluer, Influence of supplementary cementitious materials on the performance and environmental impacts of reactive magnesia cement concrete, Journal of Cleaner Production 159 (2017) 62-73.
[25] M. Atkins, F. Glasser, J. Jack, Zeolite P in cements: its potential for immobilizing toxic and radioactive waste species, Waste Management 15(2) (1995) 127-135.
[26] W. Li, P. Ni, Y. Yi, Comparison of reactive magnesia, quick lime, and ordinary Portland cement for stabilization/solidification of heavy metal-contaminated soils, Science of the Total Environment 671 (2019) 741-753.
[27] W. Li, Y. Yi, Stabilization/solidification of lead-and zinc-contaminated soils using MgO and CO_2, Journal of CO_2 Utilization 33 (2019) 215-221.
[28] H.L. Wu, D. Zhang, B. Ellis, V. C. Li, Development of reactive MgO-based Engineered Cementitious Composite (ECC) through accelerated carbonation curing, Construction and Building Materials 191 (2018) 23-31.
[29] R. Zhang, D.K. Panesar, Mechanical properties and rapid chloride permeability of carbonated concrete containing reactive MgO, Construction and Building Materials 172 (2018) 77-85.
[30] R. Zhang, N. Bassim, D.K. Panesar, Characterization of Mg components in reactive MgO–Portland cement blends during hydration and carbonation, Journal of CO_2 Utilization 27 (2018) 518-527.
[31] L. Wang, L. Chen, J.L. Provis, D.C. Tsang, C.S. Poon, Accelerated carbonation of reactive MgO and Portland cement blends under flowing CO2 gas, Cement and Concrete Composites 106 (2020) 103489.

[32] S. Ruan, C. Unluer, Influence of mix design on the carbonation, mechanical properties and microstructure of reactive MgO cement-based concrete, Cement and Concrete Composites 80 (2017) 104-114.
[33] C. Unluer, Enhancing the carbonation of reactive magnesia cement-based porous blocks, University of Cambridge, 2012.
[34] S. Ruan, J. Qiu, E.-H. Yang, C. Unluer, Fiber-reinforced reactive magnesia-based tensile strain-hardening composites, Cement and Concrete Composites 89 (2018) 52-61.
[35] S. Ruan, C. Unluer, Comparison of the environmental impacts of reactive magnesia and calcined dolomite and their performance under different curing conditions, Journal of Materials in Civil Engineering 30 (2018) 04018279.
[36] ASTM, C25-06. Standard test methods for chemical analysis of limestone, quicklime and hydrated lime, ASTM International, West Conshohocken, PA, Vol. 10, 2019.
[37] ASTM, C109-13A. Standard test method for compressive strength of hydraulic cement mortars ASTM, Philadelphia, PA, USA, 2013.
[38] ASTM, C642, Standard test method for density, absorption, and voids in hardened concrete, Annual Book of ASTM Standards 4 (2006).
[39] J. Li, Y. Zhang, S. Shao, S. Zhang, Comparative life cycle assessment of conventional and new fused magnesia production, Journal of Cleaner Production 91 (2015) 170-179.
[40] M. Spielmann, C. Bauer, R. Dones, M. Tuchschmid, Life cycle inventories of transport services Ecoinvent v 2.0, report.
[41] D. Kellenberger, H.-J. Althaus, N. Jungbluth, T. Künniger, M. Lehmann, P. Thalmann, Life cycle inventories of building products, Final report ecoinvent data v2. 0 No, 2007.
[42] A. Josa, A. Aguado, A. Heino, E. Byars, A. Cardim, Comparative analysis of available life cycle inventories of cement in the EU, Cement and Concrete Research 34(8) (2004) 1313-1320.

[43] M.E. Boesch, S. Hellweg, Identifying improvement potentials in cement production with life cycle assessment, Environmental Science and Technology 44(23) (2010) 9143-9149.
[44] ATILH, Methodology for yearly declaration of pollutant emissions in French cement industry, Hydraulic binder industries union, association technique des liants hydrauliques (in French), 2003.
[45] T. Zhang, C. Cheeseman, L. Vandeperre, Development of low pH cement systems forming magnesium silicate hydrate (MSH), Cement and Concrete Research 41(4) (2011) 439-442.
[46] F. Jin, A. Al-Tabbaa, Strength and hydration products of reactive MgO–silica pastes, Cement and Concrete Composites 52 (2014) 27-33.
[47] A.M. Neville, Properties of concrete, 4th, London: Pitman Publishing1995.
[48] P. Duxson, G.C. Lukey, J.S. van Deventer, The thermal evolution of metakaolin geopolymers: Part 2–Phase stability and structural development, Journal of Non-Crystalline Solids 353(22-23) (2007) 2186-2200.
[49] X. Lingling, D. Min, Dolomite used as raw material to produce MgO-based expansive agent, Cement and Concrete Research 35(8) (2005) 1480-1485.
[50] P. Gao, X. Lu, F. Geng, X. Li, J. Hou, H. Lin, N. Shi, Production of MgO-type expansive agent in dam concrete by use of industrial by-products, Building and Environment 43(4) (2008) 453-457.
[51] L. Mo, M. Deng, M. Tang, A. Al-Tabbaa, MgO expansive cement and concrete in China: Past, present and future, Cement and Concrete Research 57 (2014) 1-12.
[52] L. Mo, M. Deng, M. Tang, Effects of calcination condition on expansion property of MgO-type expansive agent used in cement-based materials, Cement and Concrete Research 40(3) (2010) 437-446.
[53] R. Wang, Q. Tian, S. Zhang, H. Li, A. Lu, J. Cheng, L. Li, J. Liu, Improving efficiency of calcium oxide expansive additives by polylactic acid film, Magazine of Concrete Research 68(20) (2016) 1070-1078.
[54] JTJ 034-2000. Technical specifications for construction of highway roadbases (in Chinese), 2000.

[55] C. Sonat, N. Dung, C. Unluer, Performance and microstructural development of MgO–SiO_2 binders under different curing conditions, Construction and Building Materials 154 (2017) 945-955.
[56] Y. Yi, L. Gu, S. Liu, Microstructural and mechanical properties of marine soft clay stabilized by lime-activated ground granulated blastfurnace slag, Applied Clay Science 103 (2015) 71-76.
[57] Y. Yi, X. Zheng, S. Liu, A. Al-Tabbaa, Comparison of reactive magnesia-and carbide slag-activated ground granulated blastfurnace slag and Portland cement for stabilisation of a natural soil, Applied Clay Science 111 (2015) 21-26.
[58] Y. Yi, C. Li, S. Liu, A. Al-Tabbaa, Resistance of MgO-GGBS and CS-GGBS stabilised marine soft clays to sodium sulfate attack, Géotechnique 64(8) (2014) 673-679.
[59] I.G. Lodeiro, D.E. Macphee, A. Palomo, A. Fernández-Jiménez, Effect of alkalis on fresh C–S–H gels. FTIR analysis, Cement and Concrete Research 39(3) (2009) 147-153.
[60] Z. Zhang, Y. Zhu, H. Zhu, Y. Zhang, J.L. Provis, H. Wang, Effect of drying procedures on pore structure and phase evolution of alkali-activated cements, Cement and Concrete Composites 96 (2019) 194-203.
[61] F. Jin, A. Abdollahzadeh, A. Al-Tabbaa, Effect of different MgOs on the hydration of MgO-activated granulated ground blast furnace slag paste, Proceeding of 3rd international conference on sustainable construction materials and technologies, Kyoto, Japan (2013).
[62] F. Jin, K. Gu, A. Al-Tabbaa, Strength and drying shrinkage of reactive MgO modified alkali-activated slag paste, Construction and Building Materials 51 (2014) 395-404.
[63] W. Zhu, X. Chen, L.J. Struble, E.-H. Yang, Characterization of calcium-containing phases in alkali-activated municipal solid waste incineration bottom ash binder through chemical extraction and deconvoluted Fourier transform infrared spectra, Journal of Cleaner Production 192 (2018) 782-789.

[64] E. Gallucci, X. Zhang, K. Scrivener, Effect of temperature on the microstructure of calcium silicate hydrate (CSH), Cement and Concrete Research 53 (2013) 185-195.
[65] S. Ruan, J. Qiu, Y. Weng, Y. Yang, E.-H. Yang, J. Chu, C. Unluer, The use of microbial induced carbonate precipitation in healing cracks within reactive magnesia cement-based blends, Cement and Concrete Research 115 (2019) 176-188.
[66] S. Ruan, C. Unluer, Effect of air entrainment on the performance of reactive MgO and PC mixes, Construction and Building Materials 142 (2017) 221-232.
[67] S. Özen, M.C. Göncüoğlu, Sequential formation of natrolite-group zeolites in amygdules of basaltic lavas, The Canadian Mineralogist 53(4) (2015) 757-765.
[68] S. Wang, X. Peng, L. Tang, L. Zeng, C. Lan, Influence of hydrothermal synthesis conditions on the formation of calcium silicate hydrates: From amorphous to crystalline phases, Journal of Wuhan University of Technology-Mater. Sci. Ed. 33(5) (2018) 1150-1158.
[69] K. Okano, M. Uemoto, J. Kagami, K. Miura, T. Aketo, M. Toda, K. Honda, H. Ohtake, Novel technique for phosphorus recovery from aqueous solutions using amorphous calcium silicate hydrates (A-CSHs), Water Research 47(7) (2013) 2251-2259.
[70] M.A. Shand, The chemistry and technology of magnesia, John Wiley and Sons, USA, 2006.
[71] J. Qiu, S. Ruan, C. Unluer, E.-H. Yang, Autogenous healing of fiber-reinforced reactive magnesia-based tensile strain-hardening composites, Cement and Concrete Research (2018).
[72] P. De Silva, L. Bucea, V. Sirivivatnanon, Chemical, microstructural and strength development of calcium and magnesium carbonate binders, Cement and Concrete Research 39(5) (2009) 460-465.
[73] S. Ruan, Development of reactive magnesia cement-based formulations with improved performance and sustainability. Doctoral thesis, Nanyang Technological University, Singapore, 2019.

[74] J. Ke, M. McNeil, L. Price, N.Z. Khanna, N. Zhou, Estimation of CO_2 emissions from China's cement production: methodologies and uncertainties, Energy Policy 57 (2013) 172-181.

List of Tables

Table 1 Chemical formulation (wt. %) of clay obtained from XRF

SiO_2	Al_2O_3	Fe_2O_3	CaO	MgO	K_2O	Na_2O	Others	LOI
61.02	18.85	7.87	1.73	3.03	3.40	1.27	1.47	1.43

Table 2 Mix formulations of clay samples (wt. %) and curing regimes used in this study

Group	Clay	Na_2CO_3	Quicklime	Magnesia	w/b ratio	Curing regimes
C-NC	100 %	10 % of total solids	0	0	0.34	Natural curing
L20-NC	80 %	10 % of total solids	20 %	0	0.41	Natural curing
M20-NC	80 %	10 % of total solids	0	20 %	0.41	Natural curing
C-OC	100 %	10 % of total solids	0	0	0.34	Mixed curing
L20-OC	80 %	10 % of total solids	20 %	0	0.41	Mixed curing
M20-OC	80 %	10 % of total solids	0	20 %	0.41	Mixed curing

Table 3 Inventories for the production of 1 kg of reactive magnesia

Input/emissions	Amount [6, 39]
Raw materials	
Magnesite (kg)	2.17
Water (kg)	0.01
Energy	
Coal (kg)	0.27
Electricity (Wh)	8.67
Diesel (kg)	0.54
Emissions	
CO_2 (g)	1096.54
SO_2 (g)	4.21
CO (g)	0.02
NO_x (g)	0.01
Water vapour (m^3)	1E-5
Magnesite dust (g)	0.99

Table 4 Inventories for the production of 1 tonne of Portland cement in Europe [40-44]

Raw materials	
Limestone (ton)	1.32
Clay (ton)	0.32
Sand (ton)	0.07
Iron ore (ton)	0.01
Gypsum (ton)	0.05
Water (ton)	0.53
Energy	
Coal (ton)	$5.53*10^{-9}$
Fuel oil (ton)	$1.53*10^{-9}$
Electricity (kWh)	71.92
Petroleum coke (ton)	0.1
Diesel (ton)	$9*10^{-7}$
Emissions	
CO_2 (kg)	832.61
SO_2 (kg)	0.63
CO (kg)	1.96
NO_x (kg)	1.79
Cement kiln dust (kg)	0.87
Particulate matter (kg)	0.03

Table 5 Porosity of CaO- and MgO-based clay samples

Mixture	Controlled clay samples	CaO-based clay samples	MgO-based clay samples
Porosity	-*	27.7% ± 0.3%	27.9%±2.1%

*The porosity of controlled clay samples cannot be measured as it broken into pieces in water due to its porous structure

List of Figures

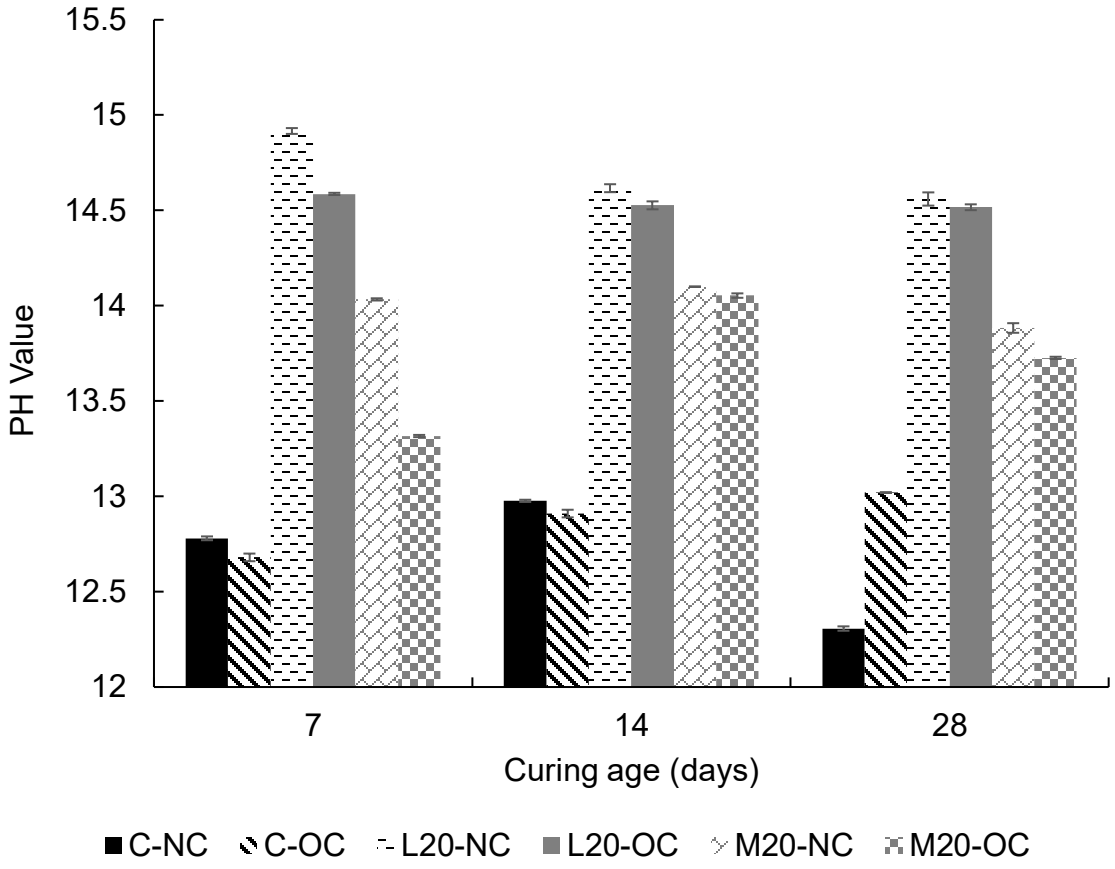

Fig. 1 pH values of the CaO- and MgO-based samples under the natural and mixed curing regimes up to 28 days

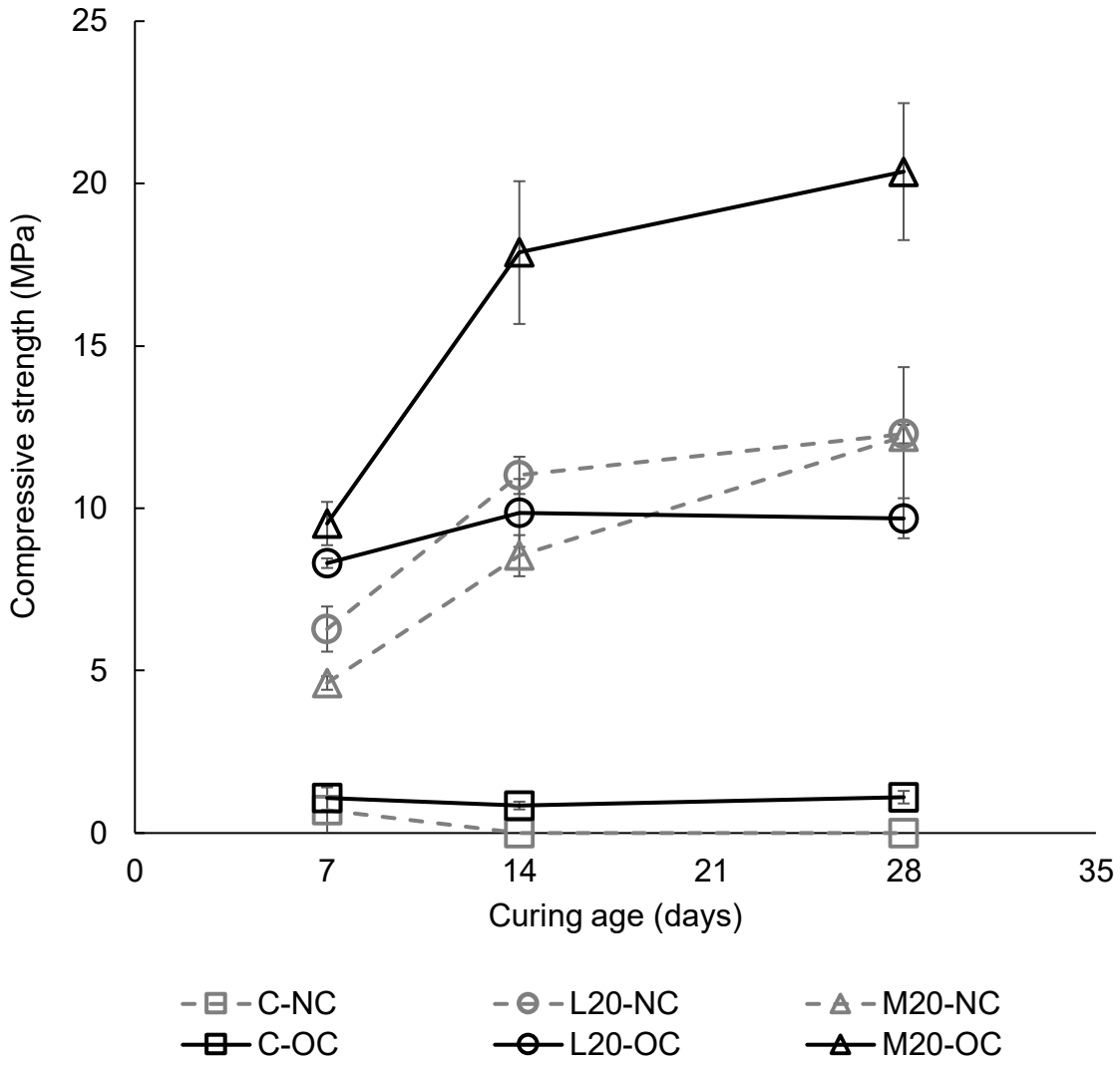

Fig. 2 Compressive strength of the control, CaO- and MgO-based groups under the natural and mixed curing regimes up to 28 days

C-NC C-OC

(a)

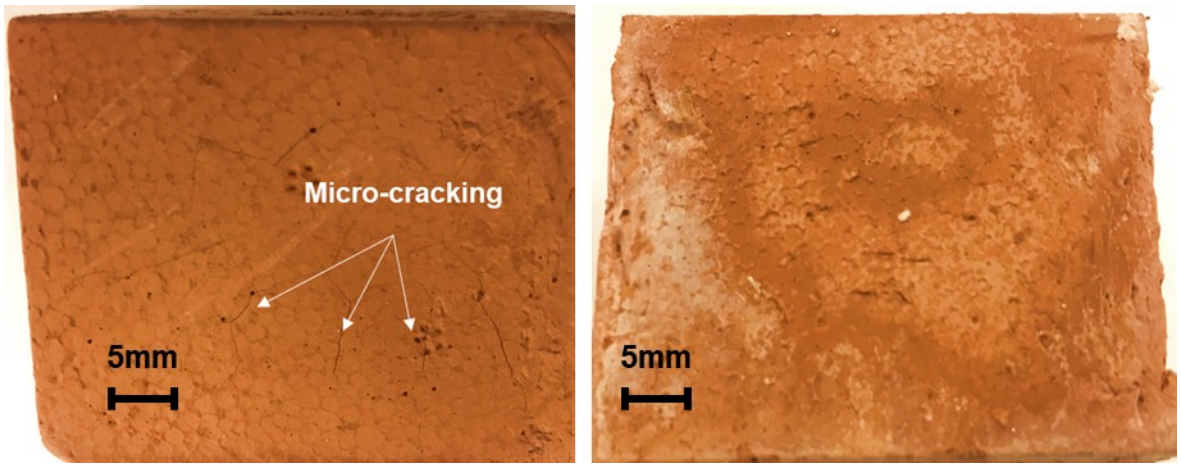

L20-OC M20-OC

(b)

Fig. 3 (a) Images of the control groups under the natural and mixed curing regimes after 7 days **(b)** Images of the L20-OC and M20-OC groups under the mixed curing regime after 28 days

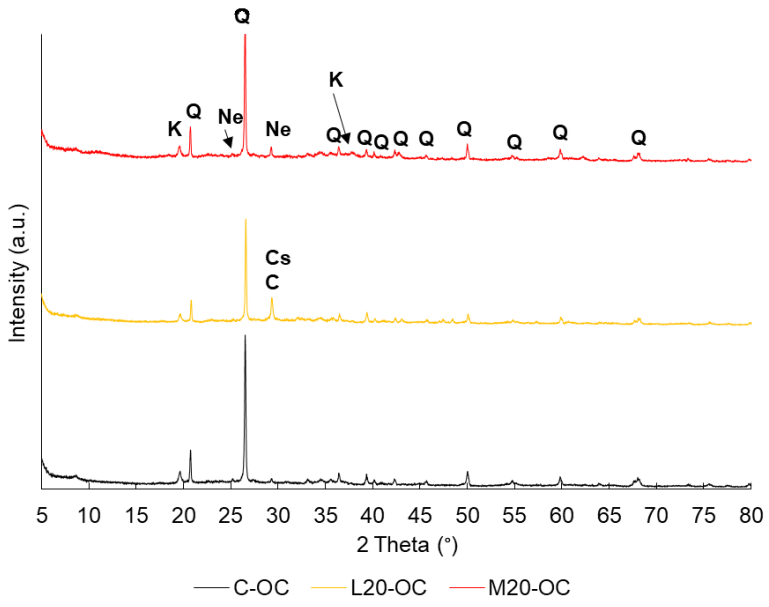

(a)

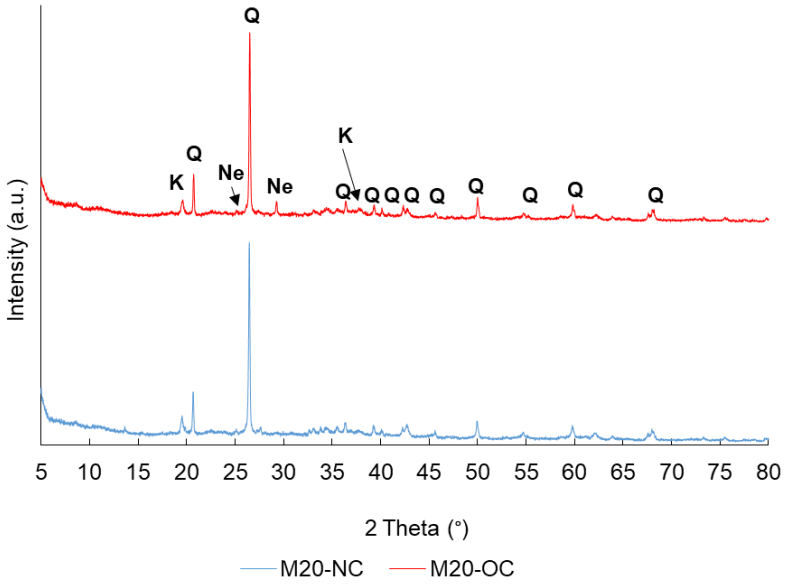

(b)

K:Kaolinite; Q:Quartz; Ne: Nesquehonite; Cs: C-S-H: C: Calcite

Fig. 4 XRD patterns of (a) selected samples under the mixed curing regime (b) the MgO-based clay samples under the natural and mixed curing regimes after 28 days

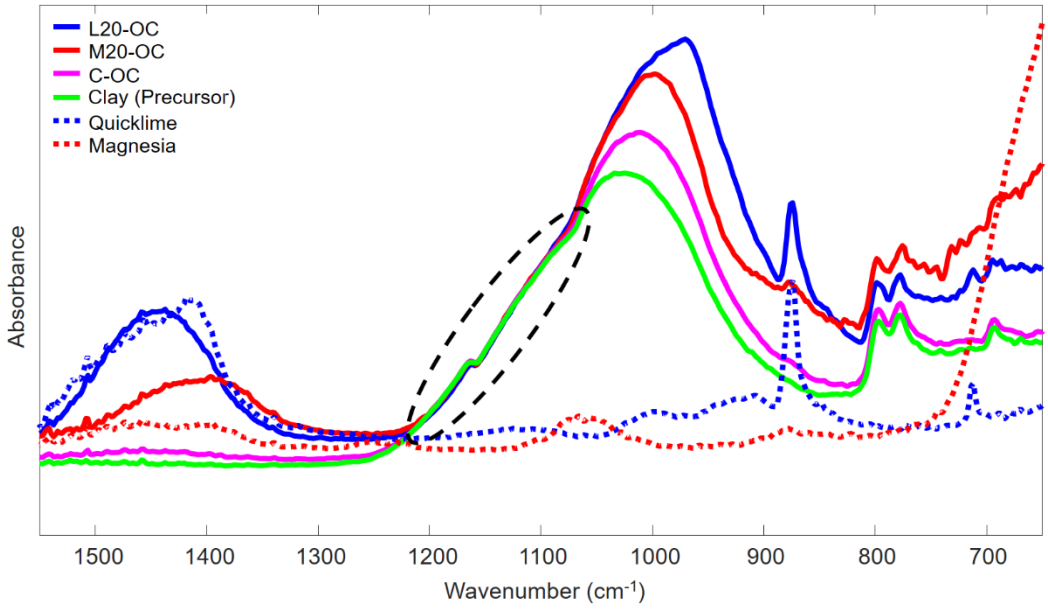

(a)

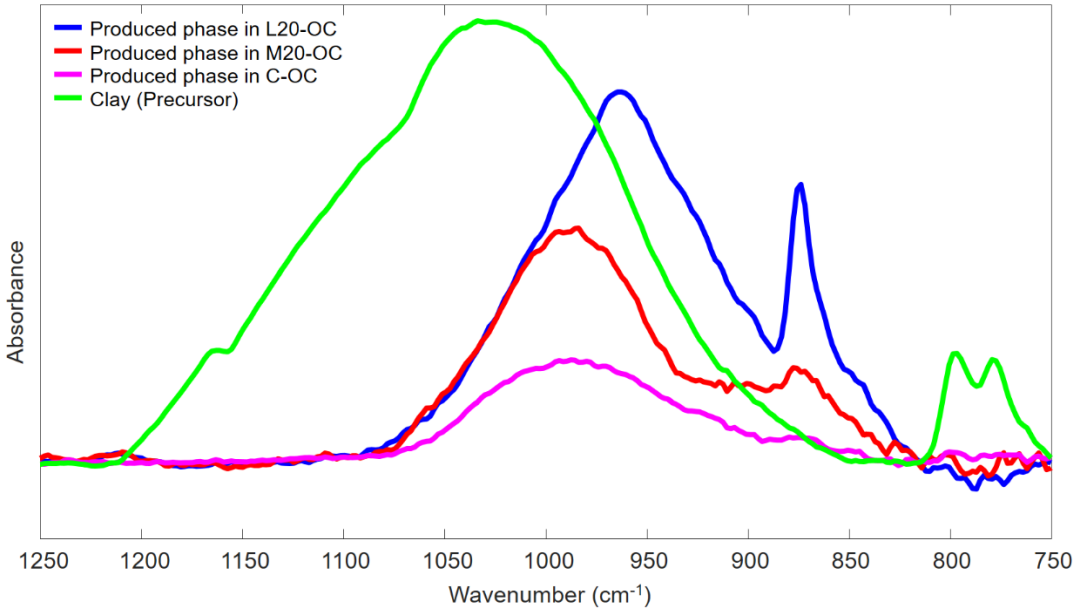

(b)

Fig. 5 (a) FTIR spectra of precursor, quicklime, magnesia and selected clay samples **(b)** subtraction of the spectra (i.e., after baseline correction) of the selected samples under the mixed curing regime after 28 days of mixed curing

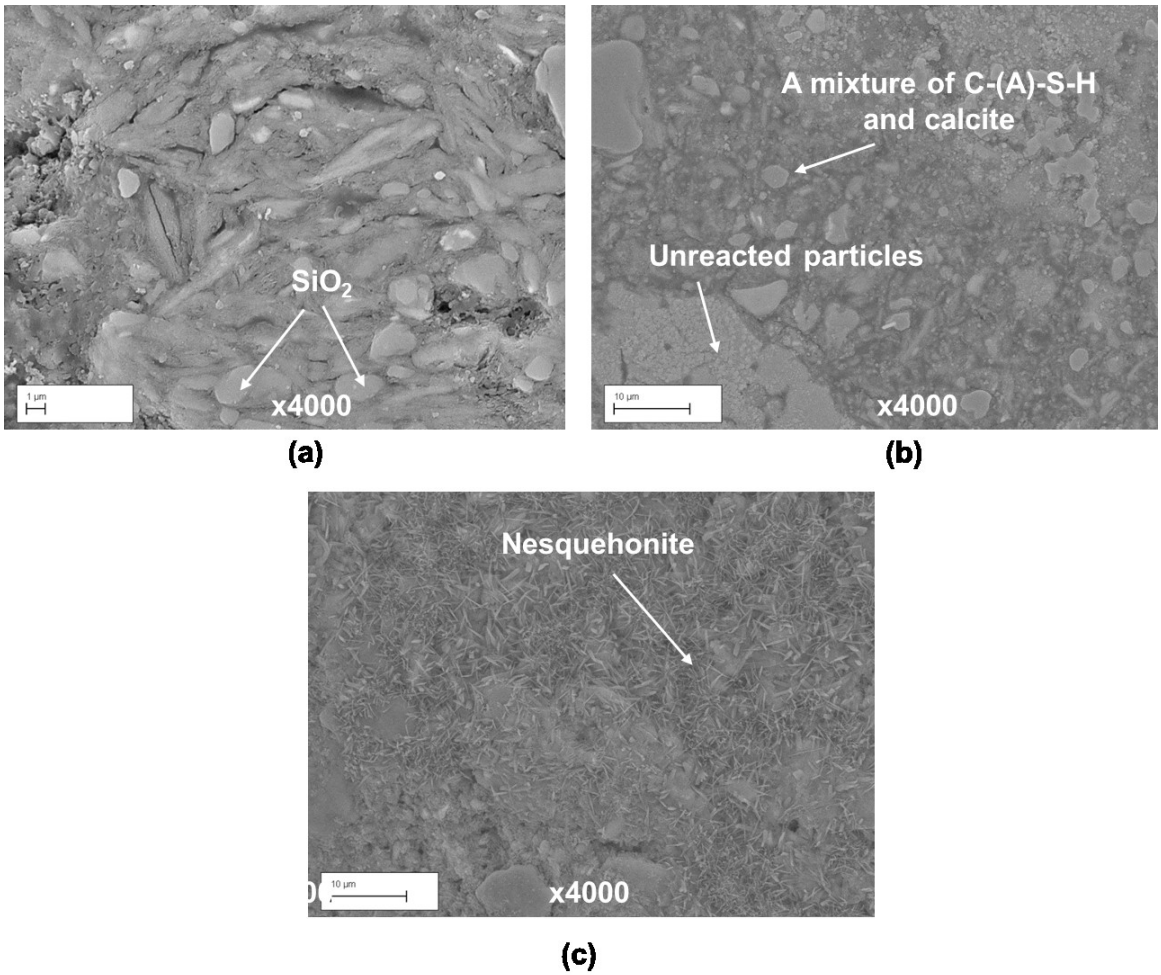

Fig. 6 BSE images of **(a)** C-OC (magnification: x4000); **(b)** L20-OC (magnification: x4000 and x10000); **(c)** M20-OC (magnification: x4000) after 28 days of mixed curing

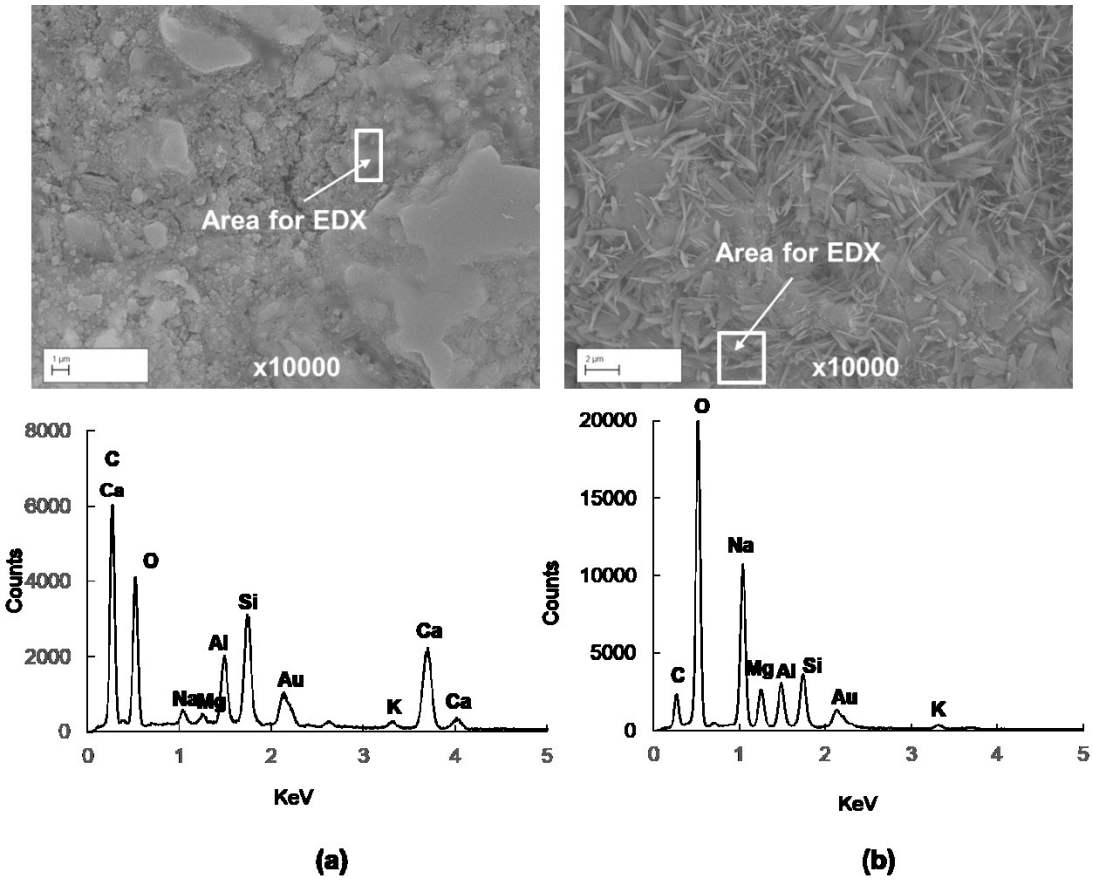

Fig. 7 Elemental spectra of selected areas in **(a)** L20-OC (magnification: x10000) and **(b)** M20-OC (magnification: x10000) after 28 days of mixed curing

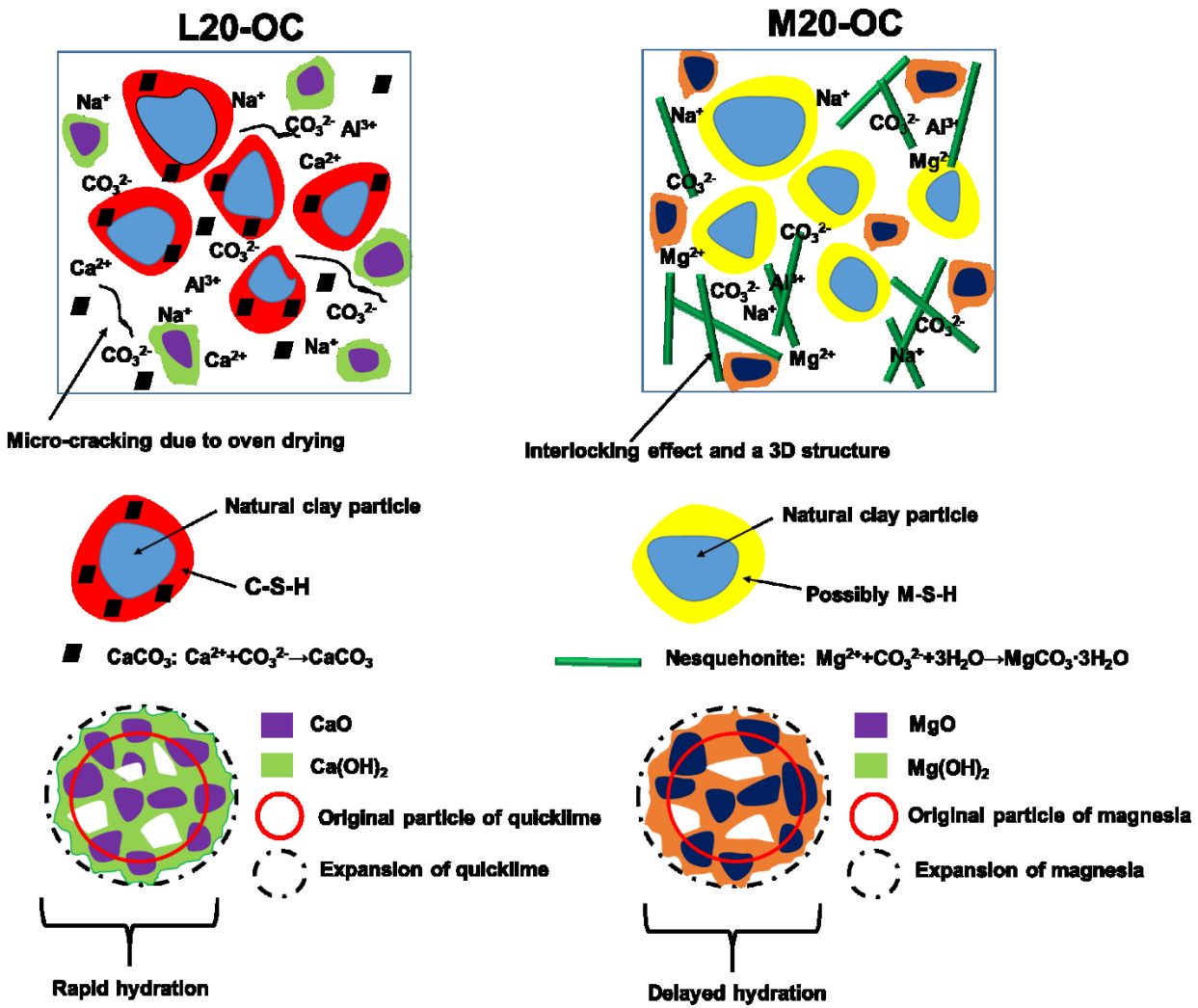

Fig. 8 Illustration of chemical reactions in the L20-OC and M20-OC groups after 28 days of mixed curing

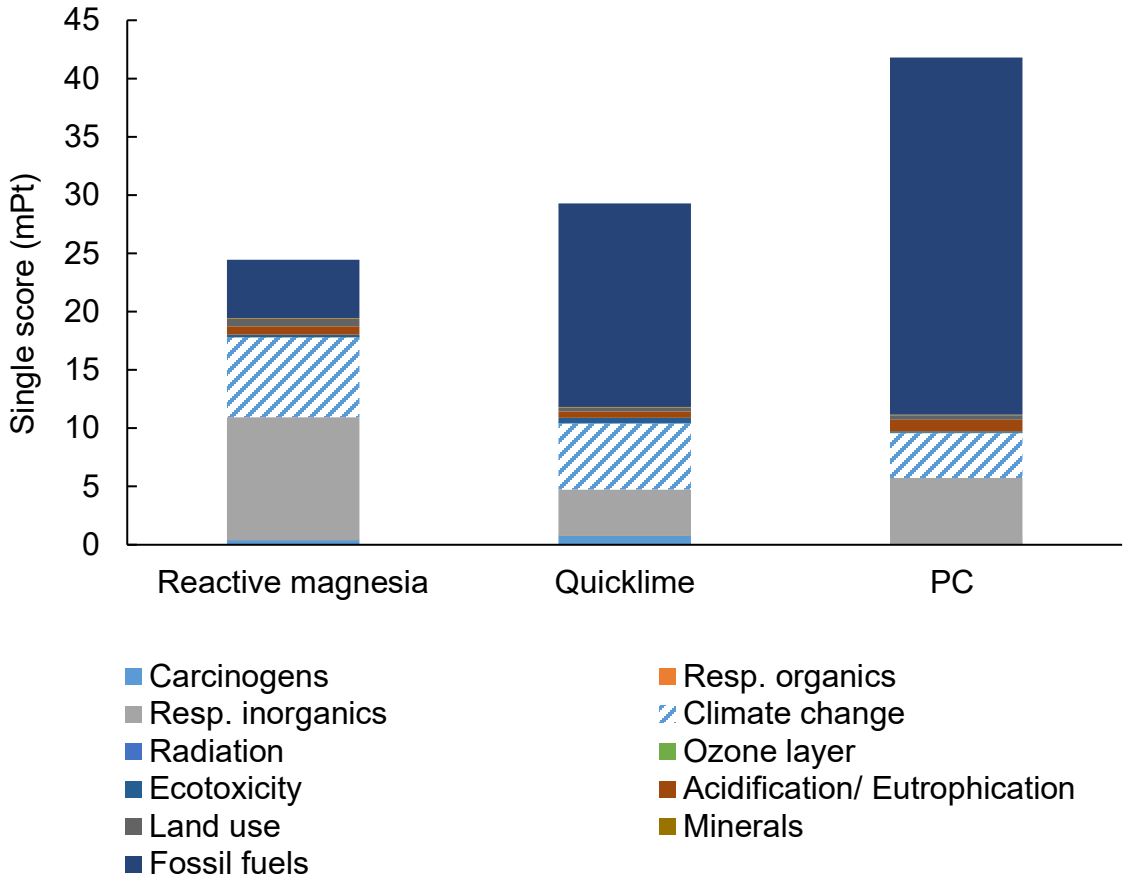

Fig. 9 Individual environmental impact of production of additive used for clay solidification